JOURNAL OF GEOPHYSICAL RESEARCH, VOL. 114, C03013, doi:10.1029/2008JC005044, 2009

Objective estimates of westward Rossby wave and eddy propagation from sea surface height analyses

C. N. Barron,[1] A. B. Kara,[1] and G. A. Jacobs[1]

Received 24 July 2008; revised 17 November 2008; accepted 13 January 2009; published 17 March 2009.

[1] An objective method to estimate westward propagation of sea surface height (SSH) anomalies is introduced and compared to a subjective technique. Both approaches use time series extracted from global SSH analyses, prepared by optimal interpolation of altimeter data, as described in detail. The cost function used in the objective method calculates the mean along-slope standard deviation, where slope is the reciprocal of propagation speed and defines the angle of linear samples through the SSH time series along each transect. The along-slope standard deviation can be computed as an extension of the Radon transform, as shown. The optimum speed estimate minimizes the cost function, and speeds with mean along-slope standard deviation within 1% of the minimum define the range of uncertainty. The 1% criteria was chosen to give a seemingly reasonable uncertainty range over a variety of cases and does not imply a specific probability that the true minimum is bounded in the uncertainty range. Applied in the central Pacific, objective speed estimates increase from 1 cm s^{-1} or less at the highest latitudes to above 30 cm s^{-1} nearer the equator. Subjective speed estimates are similar to, but generally lower than, their objective counterparts, reflecting a bias in subjective interpretation that is likely to vary among different individuals. A more detailed examination of the along-slope minimization over 160°E–95°W focuses on the higher low-latitude speeds, returning estimates of 48 cm s^{-1} (45 cm s^{-1}) at 5.5°N (5.5°S) over 1993–2006. The corresponding 42–55 cm s^{-1} (38–65 cm s^{-1}) uncertainty ranges bound most of the predictions from sensitivity test cases with alternate preprocessing filters or different multiyear time windows, although variability is larger south of the equator. The findings are consistent with prior studies and suggest the methods may be useful for other applications over the global ocean.

Citation: Barron, C. N., A. B. Kara, and G. A. Jacobs (2009), Objective estimates of westward Rossby wave and eddy propagation from sea surface height analyses, *J. Geophys. Res.*, *114*, C03013, doi:10.1029/2008JC005044.

1. Introduction

[2] The general westward propagation of ocean sea surface height (SSH) anomalies has been broadly attributed to Rossby wave activity [e.g., *Osychny and Cornillon*, 2004] even though such observations may encompass phenomena due to eddy interactions or other dynamic balances [e.g., *Chelton et al.*, 2007]. Both the zonal component of the phase velocity of Rossby waves and the overall migration of free eddies are westward, and both contribute to westward velocity trends detected in analysis of SSH time series. The approach introduced in this paper identifies the dominant phase speed of westward SSH propagation and does not distinguish between contributions from different processes. Additional observations or theoretical considerations would be needed to attribute the dominant signal in a particular region to Rossby waves, eddy drift, or other potential phenomena.

[3] Rossby waves are planetary waves that are supported by the Earth's rotation through the latitudinal dependence of the Coriolis parameter [*Gill*, 1982]. While initial identification and explanation of these waves was for the atmosphere [*Rossby*, 1939], a large body of subsequent work has considered Rossby waves in the ocean [*Emery and Magaard*, 1976; *White*, 1977; *Legeckis*, 1977; *Jacobs et al.*, 1993; *Chelton and Schlax*, 1996]. Baroclinic Rossby wave modes have phase speed dependent on the background stratification and inverse square of the Coriolis parameter. The speeds and scales of the first baroclinic mode have attracted the most research interest in the ocean [*Killworth et al.*, 1997]. Altimeter data has proved particularly useful for examining Rossby waves; some have also used infrared and ocean color measurements [*Cipollini et al.*, 1997; *Challenor et al.*, 2004]. *Killworth et al.* [1997] developed global predictions for Rossby wave phase speed and demonstrated that accounting for interaction with a mean background leads to better agreement with observed speeds, as speeds predicted by standard theory are too slow outside of the tropics.

[4] Westward migration of mesoscale eddies has received a similar level of interest in a number of ocean studies,

[1]Oceanography Division, Naval Research Laboratory, Stennis Space Center, Mississippi, USA.

complementing the work targeting Rossby waves. The interaction between eddies and the surrounding environment in the presence of the Coriolis effect produces a net westward velocity component [*Nof*, 1981; *Cushman-Roisin et al.*, 1990]. While an individual eddy may seem to emerge and disappear as it moves in and out of the pattern of altimeter ground tracks, the overall eddy tendency toward westward movement will emerge in analysis of a long time series. Satellite altimetry can help provide a comprehensive overview of the westward propagation trends over different processes, dynamical balances, and time scales.

[5] Gridded space-time distributions of SSH anomaly over most of the global ocean can be constructed from the along-track altimeter observations. These gridded fields are useful for many applications, including those discussed here. Other platforms, such as an array of ocean moorings or a series of coastal tide gauges, can provide similar space-time data distributions over limited areas. Given time series of repeat observations along an array, one can estimate the phase speed component of signals propagating along the axis of the observations; this is the westward phase speed if the measurements lie on an east-west axis. In many cases, this determination may be accomplished simply by visual inspection of a Hovmöller diagram (longitude-time plot) in which a diagonal line is drawn parallel to patterns of similar high- or low-SSH anomalies. The choice of a particular line orientation can vary according to the preferences of different analysts, perhaps leading to uncertainty or controversy that is difficult to satisfactorily resolve. In such cases an impartial, objective methodology will be a useful tool, applicable for examining overall phase speeds of Rossby waves, migrating eddies, or other phenomena.

[6] The major goals of this paper are (1) to introduce a database of daily, globally gridded SSH analyses, (2) to present an objective method that uses these fields to estimate predominant propagation speeds, and (3) to apply these data and methods to determine and compare westward propagation across the central Pacific. Such an impartial method is generally applicable over the global ocean and could be used to identify phase speeds of alternative signals in similar studies. The efficacy of using the objective method in comparison to a subjective methodology is illustrated over a series of zonal transects in the northern and southern hemispheres. We examine differences in speed estimates by the two methods, with corresponding consideration of uncertainty estimates and latitudinal variations.

[7] The organization of this paper is as follows. The coverage and processing applied to prepare along-track altimeter data is reported in section 2. Techniques and issues associated with transforming the along-track data into gridded daily global SSH analyses are introduced in section 3. Approaches for estimating phase speed are covered in section 4, including description of a proposed objective method based on minimization of along-slope standard deviation. Broader application of this objective method and comparison with subjective speed estimates are demonstrated in section 5 to determine trends of westward propagation across the central Pacific. Section 6 follows with numerous comparisons in the near-equatorial Pacific, including examination of sensitivity to different preprocessing or time windows and a survey of alternate methods with intercomparison of findings reported in earlier research. The conclusions summarize results in the context of prior studies, and an appendix provides more detail on processing the altimeter data.

2. Altimeter Data

[8] Satellite altimeters provide regularly repeating observations of SSH anomalies over the global ocean. These SSH data are an exceptional resource for observing the dynamic response of the global ocean on a range of time and space scales. The products examined here are from a Naval Research Laboratory (NRL) global hindcast reanalysis available online at www7320.nrlssc.navy.mil/modas2d/gbl.html. The SSH analyses use all available altimeter data from the operational real-time U.S. Navy Altimeter Processing System (ALPS). An overview of ALPS is provided here; additional details are given by *Whitmer et al.* [2004].

[9] The SSH fields are hindcast reanalyses of archived altimeter data from satellites in up to three exact repeat orbits: 10-day orbits for TOPEX (January 1993 to August 2002) and Jason-1 (March 2002 to December 2005), a 17-day orbit for GEOSAT Follow-On (GFO) (December 2000 to December 2005), and 35-day orbits for the European Earth Remote Sensing (ERS/Envisat) satellites (January 1995 to December 2006). Data from the Poseidon instrument colocated with TOPEX were not used because of the large gaps between repeat segments. As an example, altimeter SSH values from ALPS up to 1 November 2002 are shown in the central North Pacific in Figure 1. The data reflect a one-sided window, extending back in time up to 35 days to show the most recent measurement at each repeating observation point along the altimeter ground tracks. In the operational system, the altimeter data are generally available within 48–72 h of the observation, forcing nowcast predictions to use a biased, one-sided time window with only prior observations for nowcast analyses. Within this study the data are used in a hindcast mode, allowing time-centered treatment with no operational delays or gaps other than missing data that were never delivered or recovered.

[10] Altimeter data enters ALPS at the U.S. Naval Oceanographic Office (NAVOCEANO) as height data and orbit solutions. These inputs come from a variety of sources: NAVOCEANO directly receives GFO data and computes the required orbit solutions; the Jet Propulsion Laboratory (JPL) provides both raw data and orbit solutions for TOPEX and Jason-1 [*Chambers et al.*, 2003] and also computes an additional GFO orbit solution; ERS and ENVISAT data are provided by the European Space Agency (ESA) through the National Oceanic and Atmospheric Administration (NOAA) Laboratory for Satellite Altimetry with orbit solutions from Delft University. By the time the data are ready for ALPS, they have been transformed into geophysical data records (GDRs) which contain ancillary information used to correct for atmospheric effects and remove signals due to processes that are not of immediate interest, such as tidal variations and atmospheric pressure

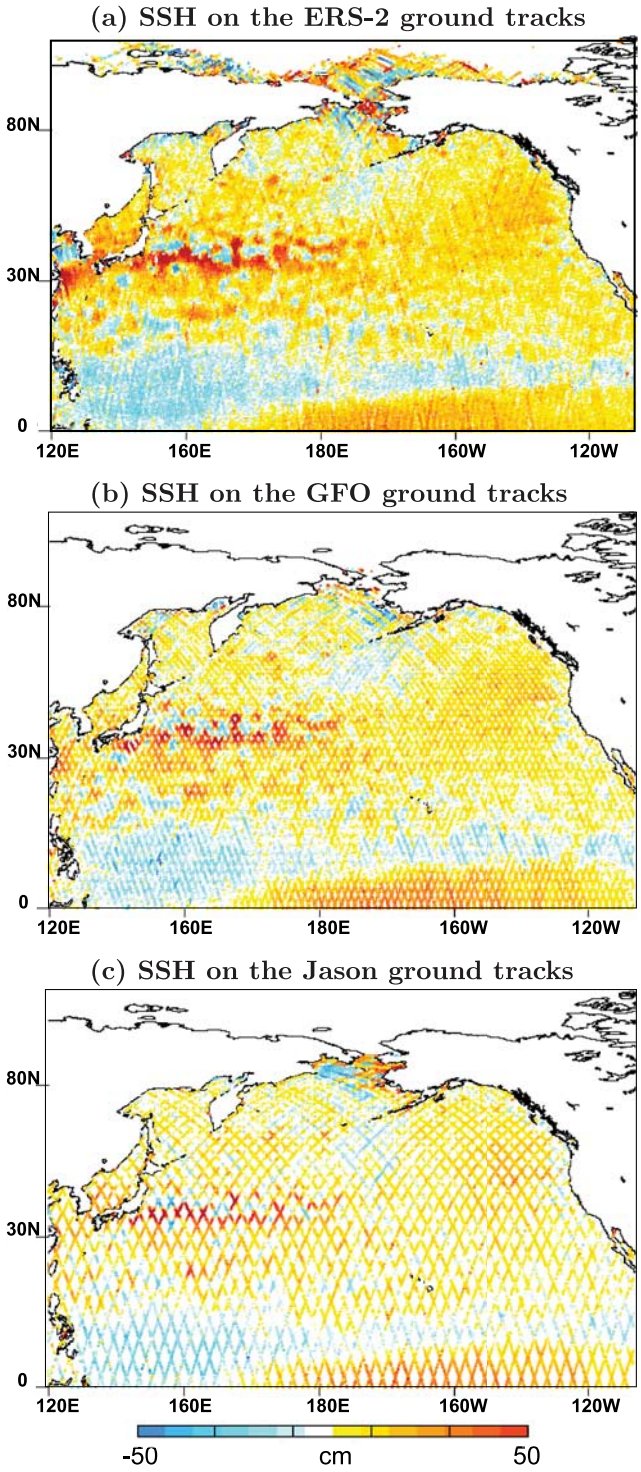

Figure 1. Snaphots from the ALPS Web page showing the most recent data up to 1 November 2002 for (a) ERS-2, (b) GFO, and (c) Jason-1. Measurements are shown in the North Pacific along the repeat ground tracks of each altimeter.

loading. More details on transformation of altimeter data within ALPS are provided in the appendix.

3. MODAS SSH Analysis

[11] Daily SSH reanalyses are constructed using all available satellite altimeter data for the global ocean spanning 80°S to 80°N. This study considers analyses from the beginning of 1993 to the beginning of 2006, covering 13 years plus 1 day or, effectively, a 13-year time series. Gridding is accomplished using tools from the Modular Ocean Data Assimilation System (MODAS) [*Fox et al.*, 2002] to produce daily fine resolution (1/4° × 1/4°, latitude × longitude grid) products. The steps for the construction of MODAS SSH from the archived data are briefly described here.

[12] ALPS prepares all the altimeter observations contributing to the gridded SSH analyses. Retrievals from ALPS represent SSH deviations from the multiannual mean SSH at each ground track location, $SSH_{altimeter}$ = altimeter measurement − ⟨altimeter measurement⟩$_{alt}$, where "⟨ ⟩$_{alt}$" refers to an averaging over the multiyear altimeter data collection period from 1993 through 2001 [*Jacobs et al.*, 2001]. Crossover points are used to reference the altimeter data to a common TOPEX mean [*Zlotnicki et al.*, 1989]. Since the observations are anomalies from a long-term mean, a mean SSH may be added from another source to form the full SSH, as described below.

[13] The primary application for MODAS SSH is prediction of synthetic subsurface temperature and salinity profiles [*Fox et al.*, 2002], which in turn are assimilated into operational ocean models [*Barron et al.*, 2004]. In this role, MODAS SSH fields are used to indicate steric sea surface height, changes in vertically integrated specific volume anomaly at constant vertically integrated mass. Thus, we attempt to retain components most correlated with subsurface temperature while minimizing other components. Since shallow regions are likely to have large nonsteric signals, perhaps because of wind-driven mass changes, altimeter observations in regions shallower than 200 m are excluded from the MODAS analyses. Beyond their primary application, these fields have also been useful for examining regional distributions of geostrophic velocity [*Boebel and Barron*, 2003].

[14] Traditionally, altimeters report time average measurements every second to give observations at about 7 km spacing along the ground track. When interpolating to a gridded field, this high-resolution along-track data must be appropriately blended across the gaps between ground tracks, which can be hundreds of km, and across intervals between repeat samples, which for a particular track may be 10–35 days, depending on the orbit. Certain mesoscale features such as small eddies may lie between tracks even when data from multiple altimeters are available. We turn to optimal interpolation (hereafter OI) in an attempt to appropriately use along-track detail, blend across time and space gaps between tracks and repeat observations, and minimize spurious features in data voids.

[15] OI has three key elements: the observations, the first guess, and the expected covariance of errors in the observations and first guess [*Lorenc*, 1981; *Barron and Kara*, 2006]. The data are SSH anomalies from the long-term

mean as reported through ALPS. Observation errors of 5–11 cm, depending on the altimeter, are assigned on the basis of 20-day running means of root mean square differences at crossover points, points where ascending and descending altimeter tracks cross and thus give two estimates of local SSH at a sampling interval shorter than the repeat period. In other words, over the short time interval between ascending and descending views of a crossover point, differences in the SSH are assumed to be due to errors. These errors may be in the measurement itself or be a representativeness error where the scale or nature of the process contributing to the signal is not resolved by the analysis. For MODAS applications, a nonsteric contribution to SSH such as a storm surge would be classified as an error term. The daily reanalysis uses a two-sided time window of ±35 days, ensuring at least two repeat observations from any orbit. To reduce the influence of correlated errors and improve efficiency, observations are averaged every 4 s, giving an along-track spatial scale of about 28 km, approximately the 1/4° spacing of the gridded fields.

[16] The MODAS SSH analyses are global. Fields from a subset region, the central North Pacific, are extracted for illustrative purposes (Figure 2). The first guess (Figure 2a) is a large-scale weighted average of the SSH observations using a Gaussian weighting with 750-km zonal, 250-km meridional, and 15-day temporal scales, all of which were chosen on the basis of subjective assessment of the resulting averages. The error covariance for the OI is also Gaussian, including advection terms with geographically variable scales determined from analysis of altimeter data by *Jacobs et al.* [2001]. First-guess errors are assigned to equal climatological standard deviation of SSH (Figure 2b). Observation increments are calculated by subtracting the first guess from the observations; these are provided to the OI which balances the representativeness and expected errors in the observations with uncertainty in the first-guess field to produce analysis innovations (Figure 2c). Adding the innovation to the first guess produces the SSH analyses (Figure 2d). As this is an anomaly field, it can be added to a mean, such as the mean climatological steric height anomaly field in Figure 2e, to estimate total SSH (Figure 2f). The OI also returns fields of expected error, which can be expressed as a nondimensional fraction of the first-guess error (Figure 2g) or as an error with dimensions of height (Figure 2h).

[17] An example of SSH anomalies processed from the MODAS analysis is provided at 43°N between longitude 170°W and 140°W in the central Pacific Ocean (Figure 3). As seen from the Hovmöller diagram, there are strong interannual variations in SSH during 1993–2006 (Figure 3). SSH anomalies of <5 cm in the early months of 1996, 1997 and 1998 at most longitudes reach higher values for the next 4 years until 2003. There are also relatively high SSH anomaly values of >5 cm during the second part of the years from 1999 through 2003. A 30-day (actually ±15 days or roughly 1 month) running average (boxcar filter) is applied to reduce noise for plotting purposes, although high-frequency noise is not a significant problem for the methods used, and the results with and without the boxcar filter are quite similar (not shown). Large-scale zonal variations in sea surface height do pose a problem, as a uniform change in SSH across the section can be interpreted as an extremely fast westward propagation. To avoid this misinterpretation, a zonal average across the section is calculated and removed daily before applying the methodologies to determine phase speed. Applying the zonal average to the SSH section at 43°N reveals cyclic variations in section-averaged SSH year by year, with magnitudes varying roughly between −5 and 5 cm (Figure 4). Removal of the daily along-section mean SSH acts to suppress correlated large-scale variations. The SSH in Figure 5 are derived by subtracting the time series of Figure 4 from the SSH in Figure 3.

4. Determining Propagation Speed

[18] Time series of daily MODAS SSH fields are used to examine westward propagation of SSH anomalies. This westward propagation may be due to Rossby wave dynamics or natural eddy migration, and either response may be modified by a background flow, such as the North Equatorial Current. The underlying geophysical response may become more easily identified by determining whether these phase velocities are consistent with expected Rossby wave characteristics or may be better attributed to other phenomena. Two methodologies for quantifying propagation phase speed are presented and discussed: a subjective methodology (section 4.1), and an objective methodology (section 4.2).

4.1. Subjective Methodology

[19] While simple to apply, subjective methods for identifying speeds of propagating features by their very nature may differ among applications and individual analysts. They are typically based on a Hovmöller diagram where the signal of interest is extracted along a section over a time series and plotted with position along the section on the x axis and time along the y axis. Propagating waves with a phase velocity component parallel to the section emerge as diagonal lines. The phase speed component along the SSH section equals the reciprocal of the slope of these patterns. This subjective approach is easily applicable to any appropriately gridded field [e.g., *Challenor et al.*, 2004].

[20] For a latitude section plotted with longitude increasing toward the right and time increasing toward the top, eastward phase velocity produces patterns sloping upward from left to right [e.g., *Dunkerton and Crum*, 1995], while patterns due to westward propagation slope upward from right to left. Westward propagation is evident in the patterns within Figure 5, where the three solid diagonal lines are drawn according to the subjective determination of an image analyst, the lead author for the results in this paper. Another analyst would likely draw a different set of lines. Note that the diagonal patterns are less evident in Figure 3, which shows strong seasonal and interannual variation of mean elevation that obscures westward propagation of SSH anomalies. When the zonal averages shown in Figure 4 are removed, propagating SSH features are more easily identified. The reciprocals of the slope of these solid lines give the phase speed of westward propagation. A horizontal line (zero slope) indicates infinite phase speed, while a vertical line would correspond to zero phase speed. Identifying multiple lines increases confidence in the mean and provides a range of uncertainty for the phase speed estimate. Three or more subjective estimates were completed for each section before calculating the objective estimates or even

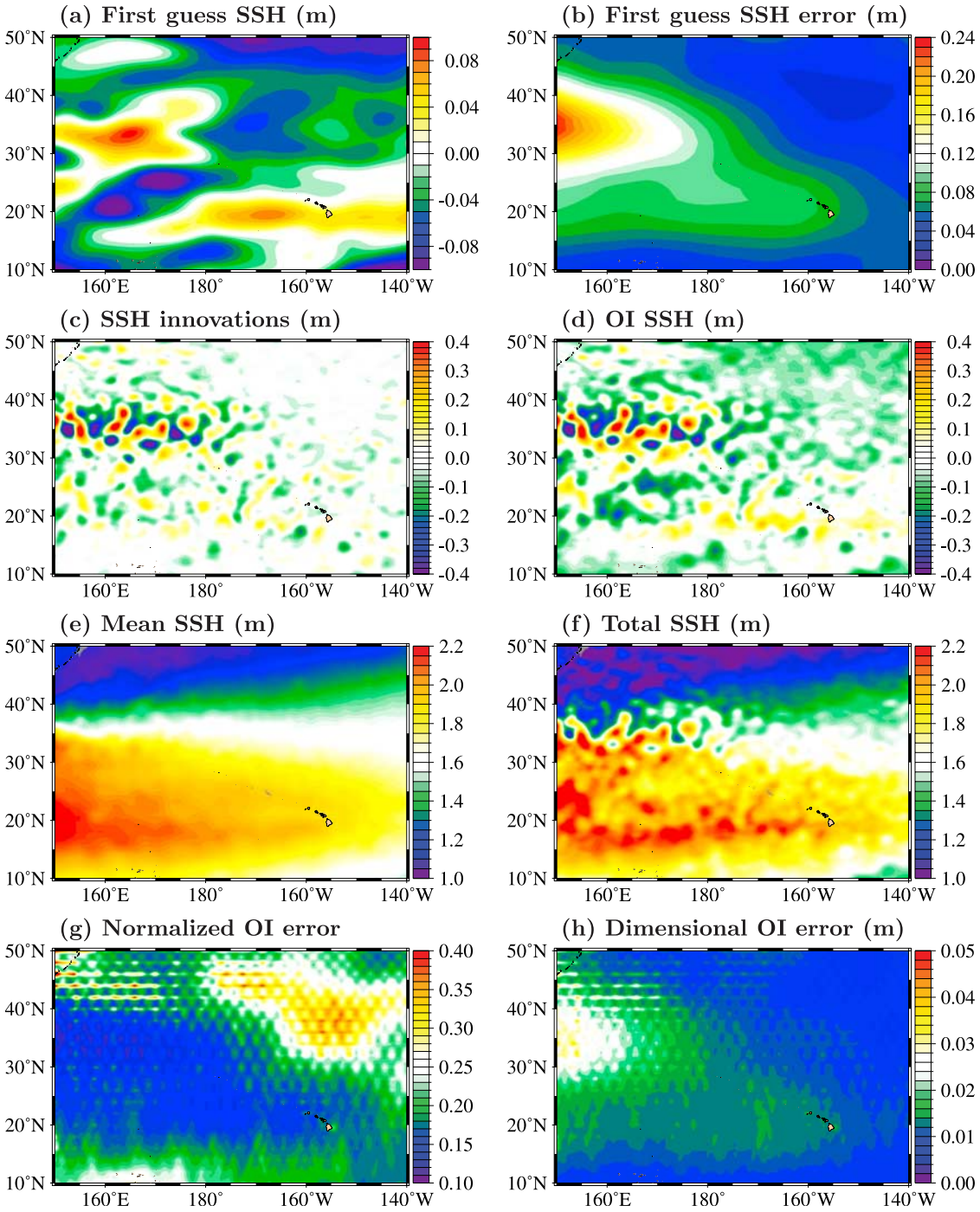

Figure 2. Steps in forming the daily MODAS SSH reanalysis OI in the central North Pacific on 1 January 2004: (a) first-guess SSH, (b) first-guess SSH error, (c) innovations resulting from OI of the altimeter SSH observations, (d) OI SSH (first guess plus innovations), (e) mean SSH defined by the mean MODAS climatological steric height anomaly relative to 1000 m, (f) total SSH (OI plus mean), (g) normalized OI error (fraction of first-guess error), and (h) dimensional OI error. Details for each image are provided in the text descriptions.

converting the slopes to speed, in order to remove any potential influence on the analyst's choices.

4.2. An Objective Methodology

[21] In this section, we present a new methodology for objectively determining the predominant phase velocity of SSH propagation. This method is based on minimizing mean along-slope standard deviation in a Hovmöller diagram. It is shown that this method can be expressed as an extension of the standard Radon transform [*Deans*, 1983]. Phase speeds determined using this objective method, for convenience called along-slope minimization, are compared

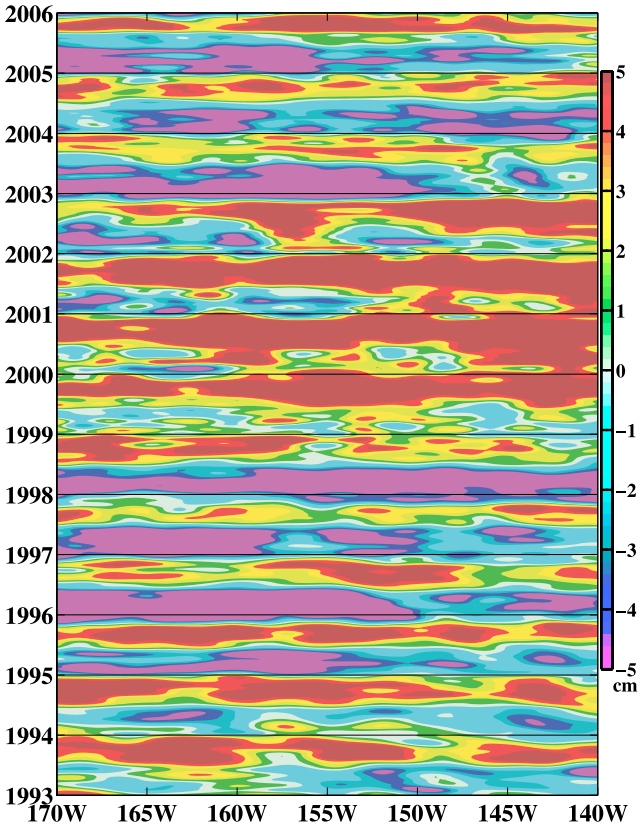

Figure 3. Interannual variations of SSH anomaly (cm) along a 43°N section from 1993 to 2006. The SSH field is extracted from the daily MODAS reanalysis time series, as described in the text. A 30-day boxcar filter has been applied to the original SSH anomalies.

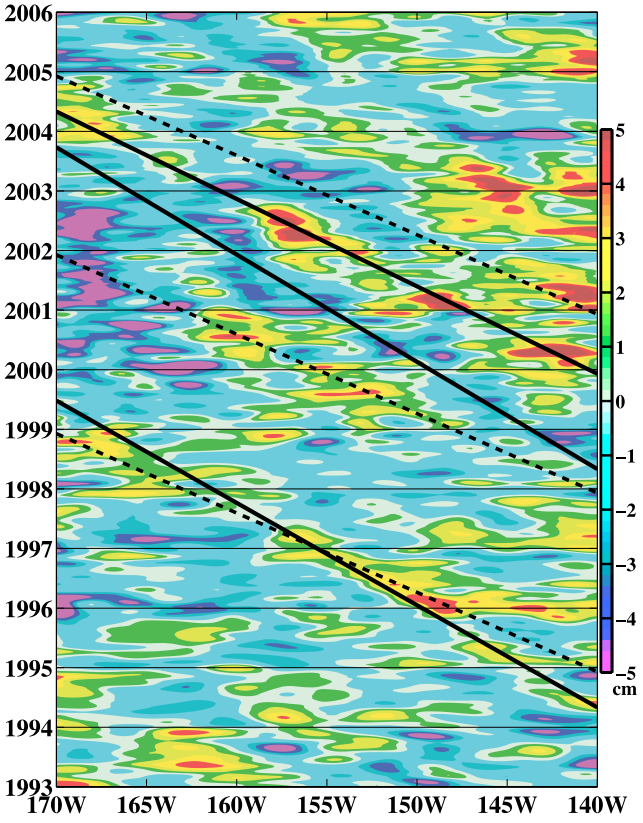

Figure 5. The same SSH anomaly field as in Figure 3, but daily zonal averages (Figure 4) are removed (i.e., mean SSH along this section is set to zero each day). Westward propagation at 43°N is identified by the slope of dashed (solid) lines based on the objective (subjective) determinations of phase speed.

with subjective estimates determined as described above. Alternate objective approaches include methods using complex singular value decomposition [*Susanto et al.*, 1998], lagged maximum cross correlation of empirical orthogonal functions (EOFs) [*Chelton et al.*, 2003], or a Radon transform of an SSH time series [*Challenor et al.*, 2001; *Chelton et al.*, 2003].

[22] As noted, the along-slope minimization examined here can be expressed as an extension of the Radon transform and is similar in some respects. It is applied in a way that conveniently provides an estimate of phase speed uncertainty, addressing an issue found in the prior objective methods. Those interested can find the MATLAB version of the code at www7320.nrlssc.navy.mil/modas/pubs.html. A detailed description of the methodology is provided here.

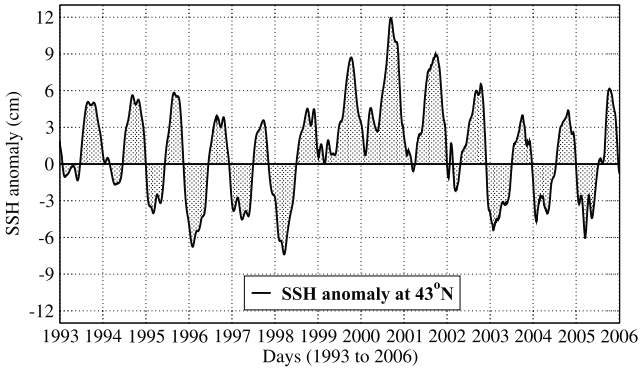

Figure 4. Zonal averages of the SSH anomaly field shown in Figure 3.

[23] Consider application of the along-slope minimization over the section time series at 43°N across 170°W–140°W during 1993–2006 as given in Figure 5. SSH values have been processed using a 30-day boxcar filter after removing the zonal mean SSH each day. This gives a two-dimensional field of SSH as a function of longitude and date. In general, the method is applicable for a generic two-dimensional field with axes of distance along the section versus time of observation. As with multiple Radon transforms, the along-slope minimization examines the field over a series of angles or slopes; the tangent of the angle is the ratio of time interval divided by distance along the section, or, as noted before, the reciprocal of the phase speed. For our purposes, it is convenient to express the problem in terms of slope.

[24] Since a westward phase speed is anticipated, we consider the subset of potential slopes having a positive time change divided by a negative longitude change. Given the discretization of our data set, the minimum nonzero slope amplitude would have a time change of 1 day across the entire section, or equivalently a phase speed of 30° of

longitude in 1 day, almost 3800 cm s^{-1} at 10°N. This greatly exceeds expected values for our signals of interest. Thus we reduce the problem size by restricting evaluation to more reasonable speeds less than 100 cm s^{-1}; the criteria in terms of slope varies with latitude. The maximum slope is also limited to the duration of the time series divided by half the section length, to ensure the lines calculating the cost function sample a representative portion of the domain. For a 13-year time series at 10°N, this corresponds to a minimum speed of less than 0.1 cm s^{-1}.

[25] Each slope is coupled with a series of intercepts along the time axis spaced at 1 day intervals to define a set of line segments through the Hovmöller diagram. Only segments spanning at least half of the width of the section are retained to calculate the mean, again to ensure that the mean is not biased by less representative segments that sample only a small portion of the space-time domain. SSH standard deviation is calculated along each line segment, and each segment is weighted equally in calculating a mean standard deviation for the slope, or equivalently, a mean standard deviation as a function of phase speed.

[26] The optimum phase speed estimate minimizes the mean along-slope standard deviation. If all signals contributing to SSH anomalies propagated westward with the same constant phase speed, then the minimum standard deviation would be zero; that is, an observer moving westward at the optimum speed would see constant SSH. As the observed SSH is a collection of various signals and errors with different characteristics, the minimum in practice is always somewhat greater than zero.

[27] The along-slope minimization can also be defined as a modification of the Radon transform. The standard Radon transform can be expressed as

$$R[f](r,\theta) = \int_{-\infty}^{\infty} f[x(r,s,\theta), t(r,s,\theta)]ds \tag{1}$$

where x and t define a linear sample projected through the time series $f(x, t)$ at an angle θ counterclockwise from direction of increasing x,

$$x(r,s,\theta) = -r\sin\theta + s\cos\theta + \bar{x} \tag{2}$$

$$t(r,s,\theta) = r\cos\theta + s\sin\theta + \bar{t} \tag{3}$$

Coordinates s and r define an orthogonal coordinate system rotated by an angle θ counterclockwise from the original x, t coordinate system and centered in the x, t field at $\bar{x}$, $\bar{t}$. Prior studies using a Radon transform approach have identified θ for which

$$\int_{-\infty}^{\infty} f^2[x(r,s,\theta), t(r,s,\theta)]ds \tag{4}$$

is maximum. A determination of the average along-slope standard deviation can be expressed as a modified Radon transform,

$$R_{NRL}[f](r,\theta) = \left\{ \frac{1}{L(r,\theta)} \int_{-\infty}^{\infty} \left\{ f[x(r,s,\theta), t(r,s,\theta)] - \bar{f}(r,\theta) \right\}^2 ds \right\}^{-1/2} \tag{5}$$

where

$$\bar{f}(r,\theta) = \frac{1}{L(r,\theta)} \int_{-\infty}^{\infty} f[x(r,s,\theta), t(r,s,\theta)]ds = \frac{R[f](r,\theta)}{L(r,\theta)} \tag{6}$$

$$L(r,\theta) = \int_{-\infty}^{\infty} \alpha(r,s,\theta)ds \tag{7}$$

and

$$\alpha(r,s,\theta) = \begin{cases} 1 & \text{where } f[x(r,s,\theta), t(r,s,\theta)] \text{ is defined} \\ 0 & \text{otherwise} \end{cases} \tag{8}$$

[28] The dominant phase speed is determined by minimizing the cost function

$$J(\theta) = \frac{1}{M(\theta)} \int_{-\infty}^{\infty} R_{NRL}[f](r,\theta)dr \tag{9}$$

where

$$M(\theta) = \int_{-\infty}^{\infty} \beta(r,\theta)dr \tag{10}$$

and

$$\beta(r,\theta) = \begin{cases} 1 & \text{where } R_{NRL}[f](r,\theta) \text{ is defined} \\ 0 & \text{otherwise} \end{cases} \tag{11}$$

[29] $L(r, \theta)$ and $M(\theta)$ normalize the integrals by the length of the samples in the s and r dimensions, respectively.

[30] Since R_{NRL} is applied to a time, space SSH time series as shown in a Hovmöller diagram, a sample at angle θ corresponds to a sample taken moving along the section at speed c. The SSH time series f along the zonal section at latitude ϕ has spatial and temporal spacing Δx and Δt, respectively. Let increasing indices i and j indicate increasing longitude and time, respectively. For θ defined as degrees counterclockwise from the $+i$ direction,

$$c = \left\{\frac{\Delta x}{\Delta t}\right\}\left\{\frac{\Delta i}{\Delta j}\right\} = \left\{\frac{\Delta x}{\Delta t}\right\}\tan(180^\circ - \theta) \tag{12}$$

[31] For the data set in this paper with $\Delta x = 0.25°$ longitude and $\Delta t = 24$ h,

$$\Delta x = 0.25^\circ \text{ longitude} \approx 0.25 \times 111\cos\phi \text{ (units km)} \tag{13}$$

so

$$c = 32.2\cos(\phi)\tan(180^\circ - \theta) \text{ (units cm s}^{-1}\text{)} \tag{14}$$

Note that a time series with different grid spacing would have a different scaling factor in equation (14).

[32] Figure 6 depicts the minimization for the SSH time series at the 43°N section previously shown in Figure 5. The minimum mean along-slope standard deviation of 1.691 cm corresponds to an optimum phase speed of 1.7 cm s^{-1}, shown as the bold dashed black line. Note that the very

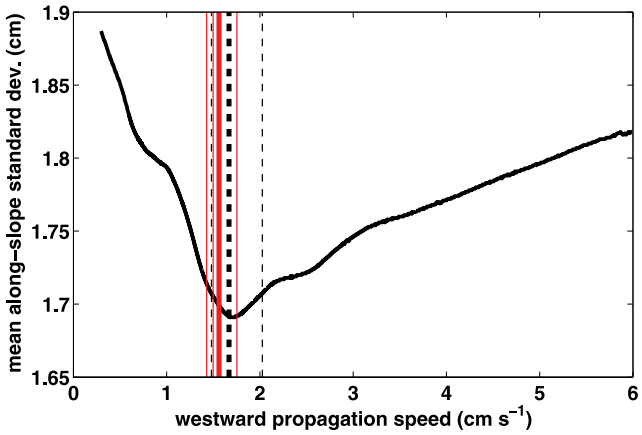

Figure 6. Minimization of mean along-slope standard deviation time series at 43°N (from Figure 5). The bold dashed line at the cost function minimum identifies the optimum phase speed, while thin dashed black lines denote a range of uncertainty. For comparison, subjective speed estimates are shown by thin solid red lines and their mean is shown as a bold solid red line.

large sample size (more than 4000 lines) over the 13-year time series enables the mean to be stated with greater precision than the individual observations. The uncertainty in the estimate is defined by cost function values within 1% of the minimum, i.e., values lower than 1.01 times the minimum. Thus, in the sample case any slope with a mean along-slope standard deviation no greater than 1.708 cm is sufficiently close to the minimum and is considered a reasonable estimate of the westward propagation speed. This gives an error range between 1.5 and 2.0 cm s^{-1}, as indicated by the thin dashed black lines. The subjectively determined speeds are shown in solid red lines for comparison, with the bold solid red line indicating their mean. At 43°N, the mean subjective speed is 1.6 cm s^{-1} and falls within the range of uncertainty of the objective method. One of the three subjective estimates falls outside of the objective uncertainty range and could therefore be identified as a poor estimate of the average phase speed that is representative of the complete time series. In this way, the objective uncertainty range gives us a basis for quality control and interpretation of other data.

5. Westward Propagation Over the Central Pacific

[33] Further comparisons of the subjective and objective speed estimates provide a more robust examination of consistency and bias for a variety of latitudes over a fairly long time period. In this way, we also develop a consistent set of estimates for the predominant speeds of westward propagation over the central Pacific. These two methods are applied to a series of zonal sections between 50°S and 50°N, all spanning longitudes 170°W–140°W over the years 1993–2006. As before, the SSH time series extracted from the global MODAS SSH analyses are prepared by removing daily mean zonal elevation and applying a 30-day running time average boxcar filter.

[34] Moving south from the initial section but remaining in the north Pacific, time series of SSH anomalies at 25°N and 35°N are shown in Figures 7a and 7b. The slopes of the subjectively determined line segments, represented by solid black diagonal lines, decrease as sections move south from 43°N (Figure 5). As line slope is inversely proportional to westward phase speed, a decrease in slope indicates an increase in speed. Thus, the trends match our expectations that phase speed increases toward the equator, or equivalently, increases as the plane of propagation is displaced farther from the Earth's axis of rotation.

[35] The cost function minimizations that objectively estimate propagation speed are illustrated by bold black dashed lines in Figures 7c and 7d. The optimum (uncertainty range) estimates are 5.9 cm s^{-1} (5.3–7.0 cm s^{-1}) at 25°N and 2.8 cm s^{-1} (2.5–3.3 cm s^{-1}) at 35°N. Thin dashed black lines denote the uncertainty range, defined as the speeds where the cost function values reach 1.01 times its minimum.

[36] The probability distribution indicated by the objective estimates is skewed relative to phase speed (right-skewed), so that the most likely phase speed estimate (cost function minimum, assumed to be the mode) is shifted toward the slower side of the uncertainty range. Plotting the along-slope standard deviation cost function relative to propagation speed contributes to the skewed distribution. If the cost function is plotted relative to slope angle, with angle decreasing (speed increasing) toward the right, the skewness shifts toward the left. For example, consider representing skewness as the ratio |mode − left uncertainty bound|/(uncertainty range). In Figure 7a, the range minimum, mode, and range maximum in terms of speed (5.3, 5.9, and 7.0 cm s^{-1}) correspond to slope angles 11.3°, 10.2° and 8.6°, respectively. Thus, while in terms of speed the skewness representation is 35%, in terms of angle it is 41%, shifting the right skew toward the center. Transformation from propagation speed to slope angle for Figure 7b produces a leftward shift in the skew ratio from 37% to 43%.

[37] The subjective speed estimates tend to be a bit slower than the objective estimates, with a mean (range of estimates) of 5.3 cm s^{-1} (4.9–5.4) at 25°N and 2.6 cm s^{-1} (2.4–2.7) cm s^{-1} at 35°N. Bold (thin) solid red lines indicate the subjective estimates in Figures 7c and 7d. While the subjective means fall within the range of objective speed uncertainty, they do indicate that the analyst making the subjective choices considered in this paper tends to identify slopes with a slow bias relative to the objectively determined optimum speed estimates.

[38] This should not imply that subjective determinations by any given analyst will always identify slower phase speeds. In fact, one of the reviewers used the plots in the paper to make independent subjective estimates of the slope, and the reviewer's subjective phase speed estimates tended to be relatively faster than the subjective estimates reported here. A key point is reinforced by these findings: subjective estimates may vary among analysts. The objective method provides consistent, reproducible results including estimates of uncertainty. The objective estimates can be used by themselves or to provide an impartial context for interpreting subjective estimates.

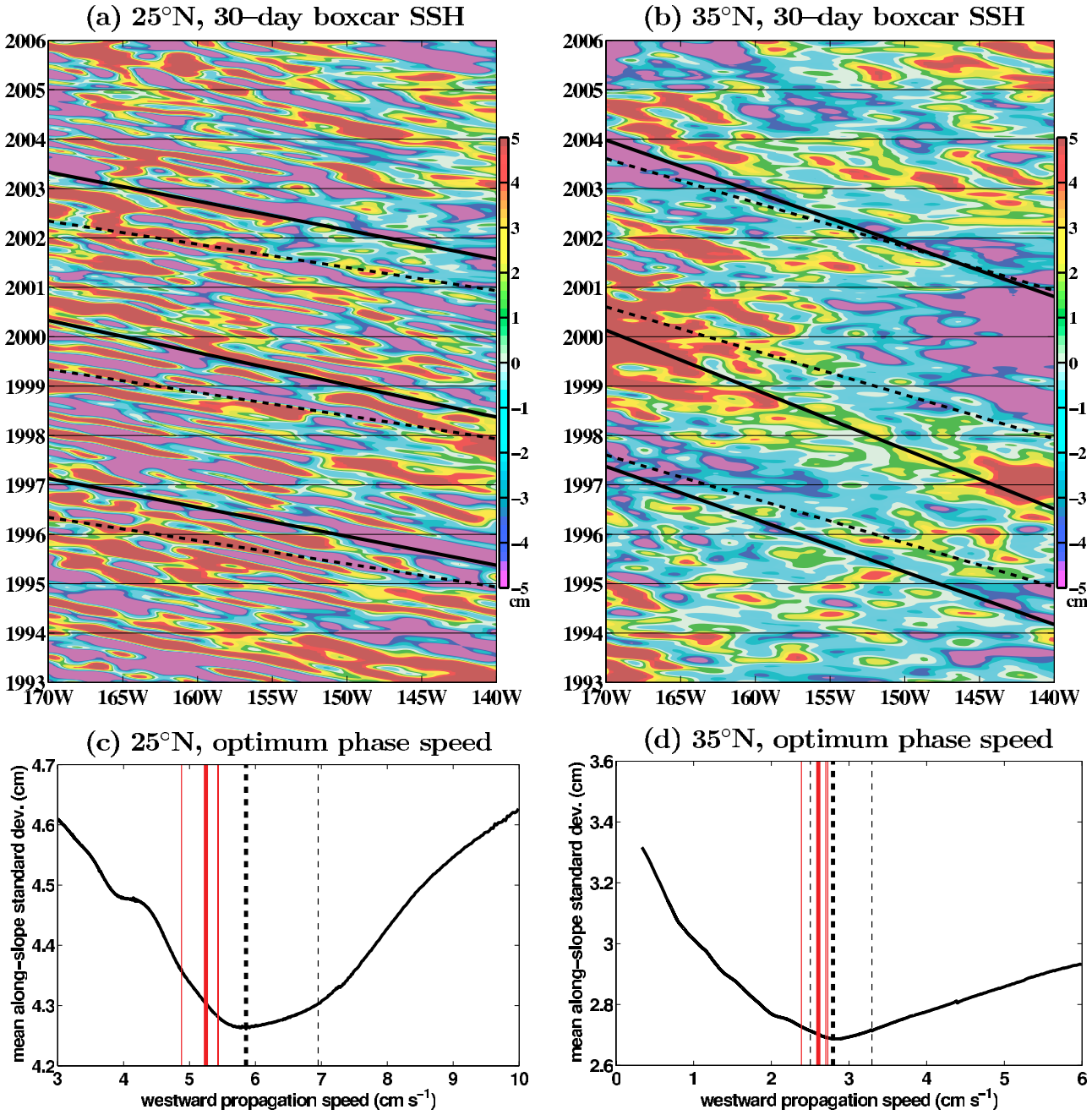

Figure 7. The SSH anomaly field in meters (30-day boxcar applied and daily zonal averages removed) from 1993 to 2006 at (a) 25°N and (b) 35°N. The slopes of the dashed (solid) lines indicate objective (subjective) determinations of phase speed. The corresponding minimization used in the objective determination at (c) 25°N and (d) 35°N. The vertical lines in black (red) indicate the results of the objective (subjective) determination of phase speed, with the bold (thin) vertical lines indicating expected values (uncertainty ranges).

[39] Similar trends are seen in the southern central Pacific. Objective estimates of the westward propagation speed optimum (uncertainty range) are 5.1 cm s^{-1} (4.6–6.7 cm s^{-1}) at 25°S and 3.7 cm s^{-1} (3.2–4.4 cm s^{-1}) at 35°S, indicated by black dashed lines in Figure 8. A bias toward slower estimates is again evident in the lines subjectively determined: 4.6 cm s^{-1} (4.3–5.0 cm s^{-1}) and 2.5 cm s^{-1} (2.4–2.7 cm s^{-1}) at 25°S and 35°S, respectively. As in the northern hemisphere cases, the optimum objective speed estimate indicated by the minimum in along-slope standard deviation is skewed toward the slower speeds in the uncertainty range. The subjective estimate mean at 35°S falls outside the objectively determined uncertainty band, indicating a significant disagreement between the objective and subjective estimates.

[40] Figure 8d reveals that the cost function signal in this section is pretty weak, 2.096 cm at its minimum. This is less than half the minimum values at 25°S (5.065 cm) or 25°N

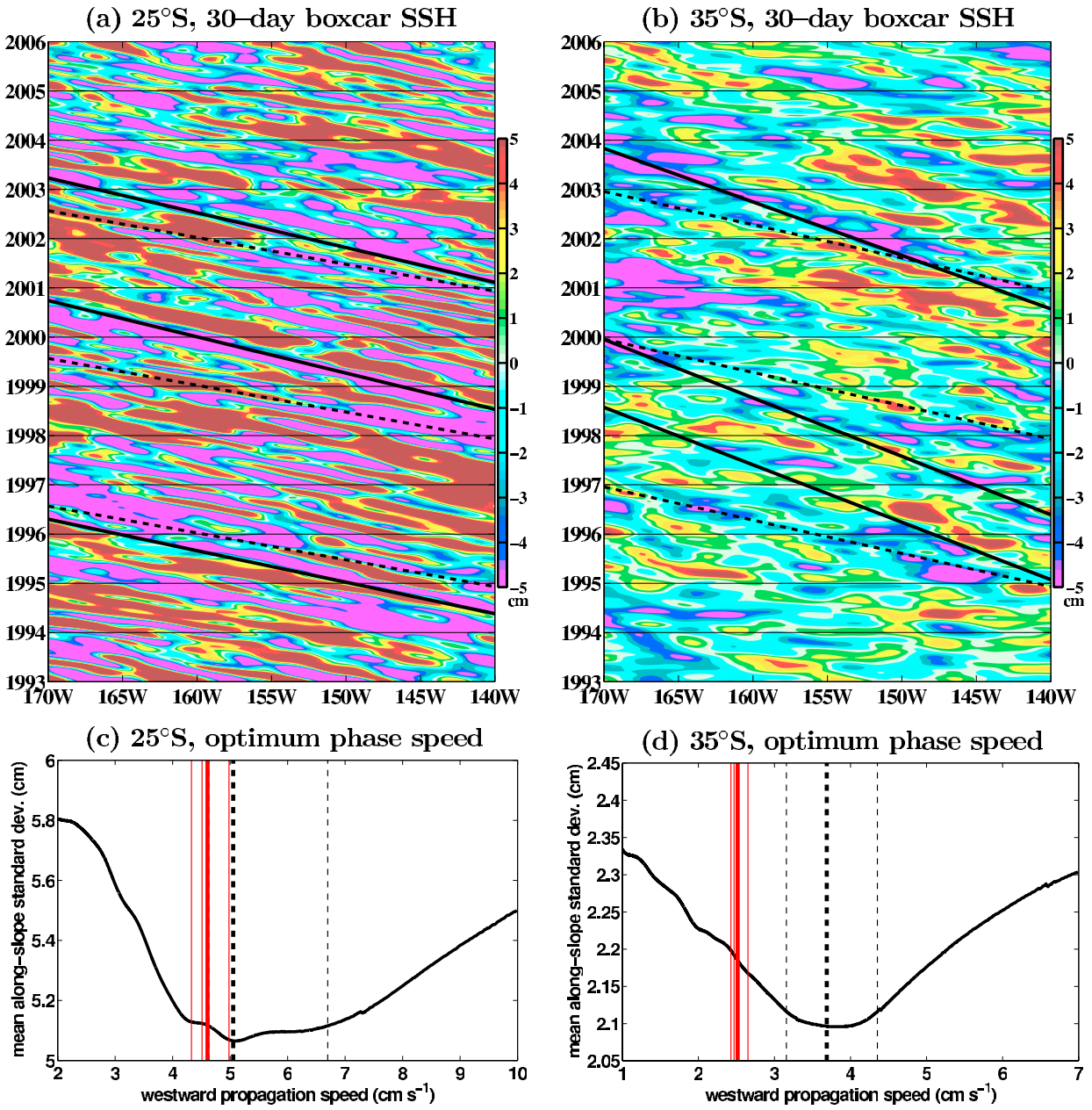

Figure 8. The same as Figure 7 but for (a and c) 25°S and (b and d) 35°S.

(4.261 cm) and significantly less than the 2.687 cm at 35°N. This implies that the low cost function range might require a larger scaling factor to define an appropriate uncertainty range. It may be that an error range defined on the basis of scaling the cost function minimum underestimates the impact of low signal strength. However, using a constant offset may poorly account for the variety of environments sampled. For example, the 1.01 scaling factor at 25°S indicates that all phase speeds with mean along-slope standard deviation less than 5.116 cm are within the expected uncertainty. We could equivalently define this as all speeds with cost function no more than 0.051 cm greater than the minimum. The 0.051 cm criteria from 25°S applied at 35°S places cost function values below 2.147 cm in the range of uncertainty, corresponding to an uncertainty range of 2.9–4.7 cm s^{-1}, rather than 3.2–4.4 cm s^{-1} using the local 1% criteria. Even though use of the constant offset in the cost function increases the uncertainty range by 50%, the larger range still does not encompass the mean of the 35°S subjective speed estimates, indicating significant disagreement between the two results. Lacking a well described probability distribution, we retain the 1.01 scaling of the cost function minimum as a useful indicator of speeds that are close to the optimal estimate, a range of speeds most

Table 1. Phase Speed Values in the Central Pacific Ocean[a]

	Objective Speed			Subjective Speed		
Latitude	Optimum	Min	Max	Mean	Min	Max
50.0°N	1.2	1.0	1.3	0.8	0.7	0.8
45.0°N	1.2	1.0	1.4	1.2	1.0	1.4
43.0°N	1.7	1.5	2.0	1.6	1.4	1.8
40.0°N	2.1	1.9	2.7	2.3	2.2	2.4
35.0°N	2.8	2.5	3.3	2.6	2.4	2.7
30.0°N	4.0	3.7	4.5	4.4	4.1	4.8
25.0°N	5.9	5.3	7.0	5.3	4.9	5.4
20.0°N	7.4	6.8	8.4	7.7	6.0	9.0
15.0°N	12.4	10.6	13.8	9.3	7.0	11.6
10.0°N	17.4	15.5	20.5	16.9	14.4	20.0
5.5°N	36.2	30.2	45.2	NA	NA	NA
5.5°S	30.5	22.9	38.8	NA	NA	NA
10.0°S	15.9	12.9	18.1	17.3	13.7	20.8
15.0°S	12.7	10.9	14.9	9.6	9.1	10.0
20.0°S	8.6	7.9	10.0	6.9	6.1	8.0
25.0°S	5.1	4.6	6.7	4.6	4.3	5.0
30.0°S	3.6	3.3	4.0	3.5	3.1	3.6
35.0°S	3.7	3.2	4.4	2.5	2.4	2.7
40.0°S	2.4	2.2	2.7	2.2	2.1	2.5
43.0°S	1.5	1.4	1.7	1.5	1.5	1.6
45.0°S	2.0	1.8	2.2	1.8	1.5	2.4
50.0°S	0.8	0.5	1.4	0.3	0.3	0.4

[a]Speed values are in cm s^{-1}. Objective optimum phase speeds minimize the along-slope standard deviations, while the minimum and maximum indicate the points where the cost function has increased by 1%. The subjective speeds reflect a mean of multiple interactive determinations of the slope over a range spanned by the subjective minimum and maximum. NA, not available.

likely including the true predominant speed of propagation over the sample transect and time interval.

[41] The objective and subjective methods to estimate propagation phase speed, described in detail above, are applied to a series of sections across the central Pacific to examine overall trends as a function of latitude. Table 1 records the results for 22 sections extending from 50°N to 50°S. Each section defines a time series of SSH from 170°W to 140°W over 1993–2006. All time series were processed to remove the daily zonal mean SSH and subjected to a 30-day running average.

[42] Subjective estimates are included for all transects except those 5.5° north and south of the equator. This pair of transects nearest the equator was added for comparisons with prior studies discussed in the next section. Subjective estimates were not made at that time to avoid introducing potential bias in the analyst's decisions, as knowledge of the earlier comparisons between the objective and subjective methods might subconsciously influence subjective choices. In addition, faster speeds produce patterns with a shallower slope in the Hovmöller diagram, and the sensitivity of speed to slope angle increases as the slope angle decreases. Faster propagation speeds near the equator lead to increased uncertainty of subjective speed estimates because of the less precise relationship between speed and slope at low slope angles on the Hovmöller diagram.

[43] In general, the uncertainty of phase speed from either approach decreases away from the equator, at least in terms of absolute magnitude (Table 1). The uncertainty of estimated speeds as a fraction of estimated speed is more constant, as estimated speeds also tend to decrease away from the equator. Figure 9 shows both objective and subjective speed estimates across the equator. As noted before, the subjective estimates tend to show a slight slow bias relative to the objective results. Occasionally this relation is reversed, e.g., at 30°N and 10°S. The largest discrepancies are noted at 15°N and 15°S; the subjective estimates here fall outside of the objective uncertainty range on the basis of a 1% increase over the corresponding along-slope standard deviation cost function minimum. Most cases show fairly good agreement between the subjective and objective speed estimates.

[44] We superimpose along-slope minimum objective speed estimates as a function of degrees of latitude from the equator to more easily visualize the symmetry or asymmetry in phase speed across the equator (Figure 10). Phase speed is fairly symmetric across the equator over most of the range but has some asymmetric deviations within 15° of the equator. Theoretical phase speeds estimates are shown for comparison. Following *Killworth et al.* [1997], the expected phase speed of nondispersive Rossby waves neglecting background currents is $-\beta C_1^2/f^2$, where f is the Coriolis parameter, $-\beta$ is the rate of change of f with latitude, and C_1 is the mode 1 internal wave speed. C_1 is interpolated from estimates of baroclinic gravity wave phase

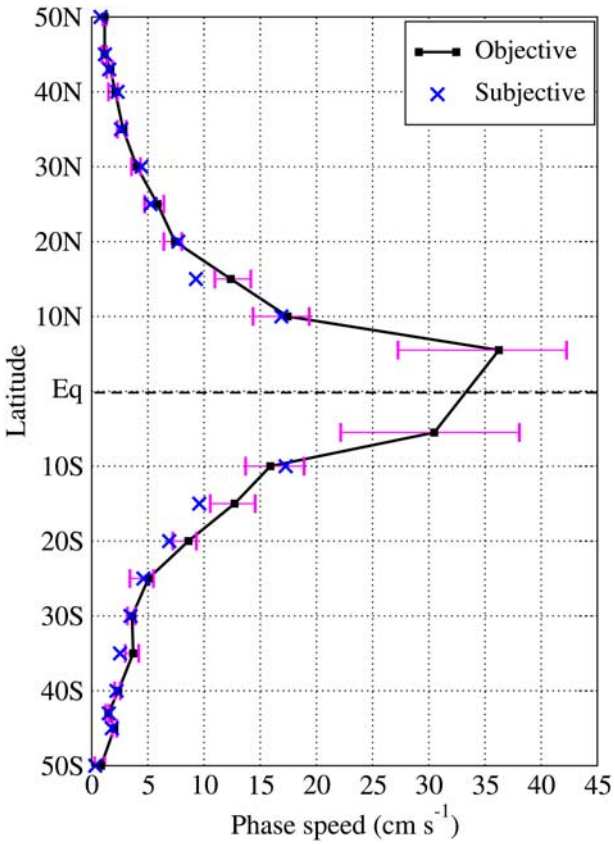

Figure 9. Comparison of estimated phase speeds determined by the subjective and objective methodologies in a series of zonal sections from 50°S to 50°N spanning the central Pacific Ocean from 170°W to 140°W. The error bars correspond to uncertainty in the objective method calculated by cost function values within 1% of the minimum.

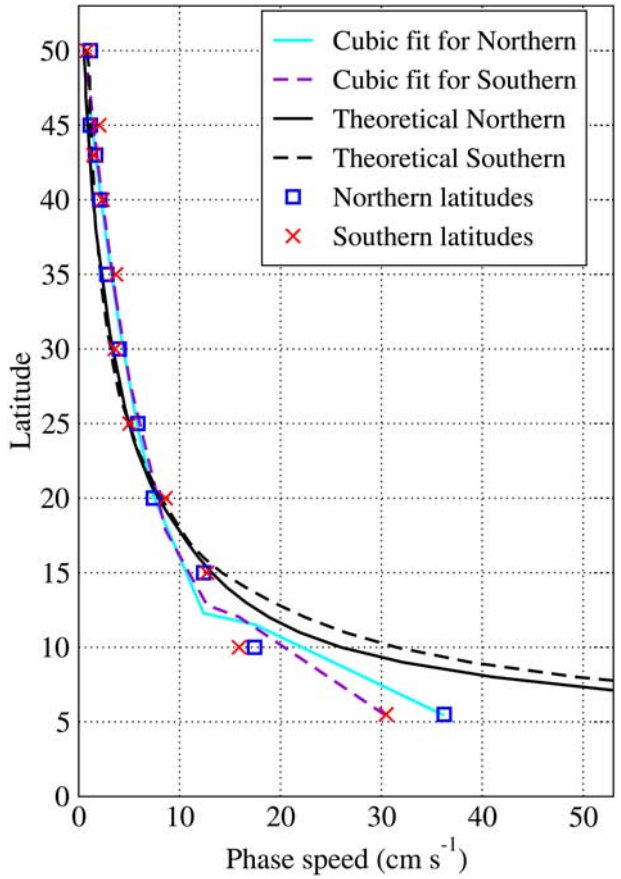

Figure 10. Objectively determined phase speeds for symmetric northern and southern latitudes are superimposed to better indicate symmetry or asymmetry across the equator and deviations from theoretical speed predictions. For example, 5° on the y axis has phase speeds for both 5°N and 5°S. The theoretical phase speed curves are $-\beta C_1^2/f^2$, following *Killworth et al.* [1997].

speed in the work by *Chelton et al.* [1998] available digitally from www.oce.orst.edu/research/po/research/chelton/index.html. Phase speeds are averaged along 170°W–140°W zonal sections at each latitude. Comparisons reveal that the objective estimates of westward propagation speed generally follow the expected latitudinal dependence for nondispersive Rossby waves, although measured speeds are generally slower than standard theory below 20° latitude and faster than standard theory above 20° latitude. Similar relationships between observed and predicted speeds have been noted by others [*Chelton and Schlax*, 1996; *Chelton et al.*, 2007], prompting *Killworth et al.* [1997] to consider the impact of mean background flows as a modification to the standard propagation theory. Our results indicate reasonable agreement with cubic polynomial functions of latitude; at this point the result is empirical without a corresponding theoretical motivation.

6. Comparisons With Other Studies

[45] A comparison with westward propagation speeds reported in prior studies serves as a final evaluation of the objective along-slope minimization method as applied to the MODAS SSH. In particular, sections near 5.5° north and south of the equator have been repeatedly examined. Results at these latitudes reported in Table 1 are based on data from 1993 to 2006 along the standard 170°W–140°W swath used so far in this paper (e.g., see Figure 5). For comparisons with other studies, we test sensitivity to alternative data selection and processing and thereby produce source data somewhat more similar to earlier work. The evaluation is extended across a broader swath of the tropical Pacific, from 160°E to 95°W. We also break the time series into shorter segments, examining spans from 1993 to 2001, 2001 to 2006, and 1993 to 2006. *Chelton et al.* [2003] covered 1993–2001, while our paper so far has included the longer interval 1993–2006. Dividing the longer span into subsets might identify speed changes over time. We also investigate sensitivity to SSH preprocessing, applying a 500-day high-pass filter in lieu of the 30-day boxcar filter. In one of their approaches to determine phase speed, *Chelton et al.* [2003] use a Loess smoother with a half span of 500 days to remove low-frequency SSH variations. Our 500-day high-pass result convolves 250-day half-width (two-sided) boxcar filters to produce a 500-day low-pass (triangle) filter [*Bowling et al.*, 2007]. Removing the low frequency leaves a 500-day high-pass signal.

[46] The MODAS SSH time series and corresponding optimum slopes for the near-equatorial comparisons are shown in Figure 11. Daily zonal means were removed to prepare the data for objective determinations of propagation speed. However, the time series displayed in Figures 11c and 11d has been subjected only to the 500-day high-pass filter; the daily means are unaltered to make the plot more suitable for comparison with a similarly processed transect in the work by *Chelton et al.* [2003]. The diagonal black lines in each plot indicate the predominant phase velocities determined by minimizing the along-slope standard deviation over the three intervals: 1993–2001 (lower two solid lines), 2001–2006 (upper two solid lines), and 1993–2006 (dashed lines). Slopes are fairly consistent over the different time periods at 5.5°N but show some noticeable changes along 5.5°S, where the slope for 2001–2006 (upper solid lines) is less steep than the others, thereby indicating a faster propagation speed.

[47] The minimizations of along-slope standard deviation for the 30-day boxcar filter cases are shown in Figure 12. Corresponding minimizations for the 500-day high-pass

Figure 11. Comparison of objective slope determination over different ranges of years for the sections examined over 1993–2001 by *Chelton et al.* [2003]. In each plot, diagonal black lines correspond to data over different multiyear spans: 1993–2001 (lower two solid lines), 2001–2006 (upper two solid lines), and 1993–2006 (dashed lines). The sections are extracted along (a and c) 5.5°N and (b and d) 5.5°S. Figures 11a and 11b (Figures 11c and 11d) have been processed by a 30-day boxcar (500-day high-pass) filter. Daily zonal average SSH is removed before determining the optimum slope, but, to facilitate comparisons, it has not been removed from the background in Figures 11c and 11d.

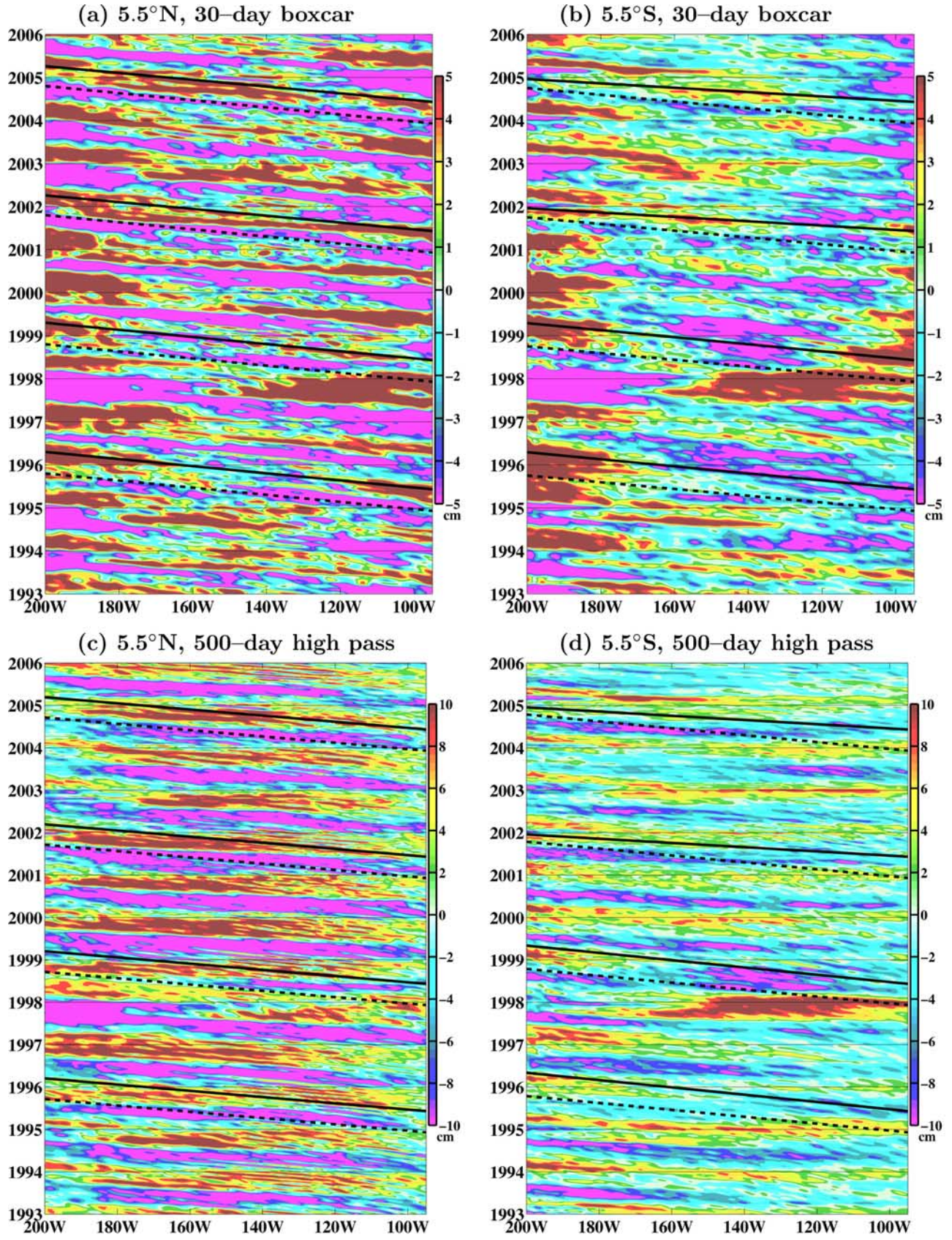
(a) 5.5°N, 30–day boxcar
(b) 5.5°S, 30–day boxcar
(c) 5.5°N, 500–day high pass
(d) 5.5°S, 500–day high pass
2006
2005
2004
2003
2002
2001
2000
1999
1998
1997
1996
1995
1994
1993
200W
180W
160W
140W
120W
100W
5
4
3
2
1
0
−1
−2
−3
−4
−5
cm
10
8
6
4
2
0
−2
−4
−6
−8
−10
cm

Figure 11

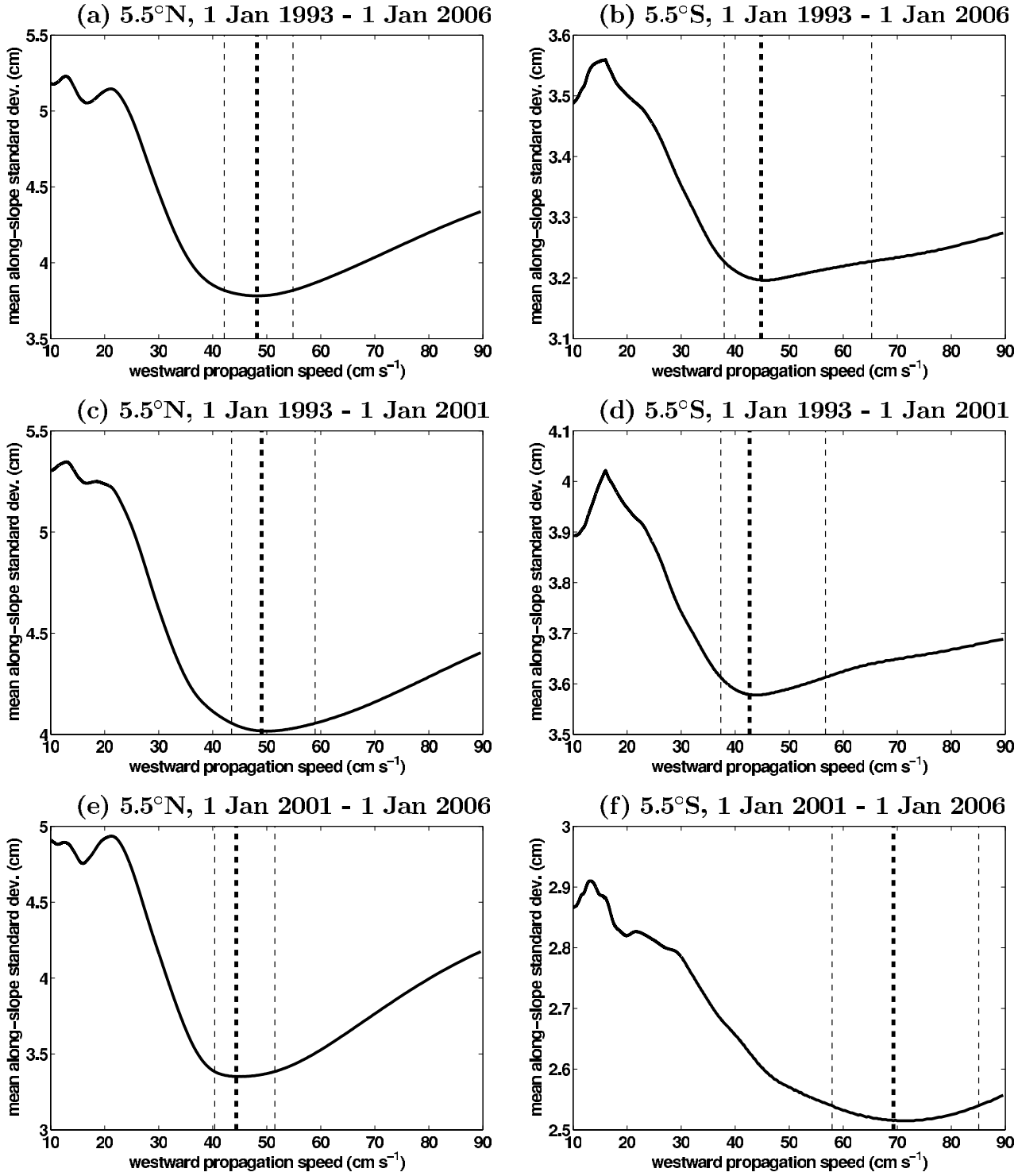

Figure 12. Minimization of mean along-slope standard deviation for the time series of sections at (a, c, and e) 5.5°N and (b, d, and f) 5.5°S. All sections shown here have passed through a 30-day boxcar filter with the daily average SSH over the section removed. Bold (thin) vertical lines indicate expected values (uncertainty ranges) determined using the objective methodology.

Table 2. Phase Speed Values Determined Over Different Time Intervals Along Near-Equatorial Sections in the Central Pacific Ocean[a]

Latitude	Optimum	Min	Max	Years	Section	Source or Variant
5.5°N	48	42	55	1993–2006	160°E–95°W	30-day boxcar[b]
5.5°N	47	41	55	1993–2006	160°E–95°W	500-day high pass[b]
5.5°N	49	44	59	1993–2001	160°E–95°W	30-day boxcar[b]
5.5°N	48	42	55	1993–2001	160°E–95°W	500-day high pass[b]
5.5°N	44	40	52	2001–2006	160°E–95°W	30-day boxcar[b]
5.5°N	42	39	52	2001–2006	160°E–95°W	500-day high pass[b]
5.5°N	36	30	45	1993–2006	170°W–140°W	30-day boxcar[b]
5.5°N	55	43	67	1994–2000	160°E–95°W	*Chelton et al.* [2003][c]
5.5°N	55	51	62	1994–2000	160°E–95°W	*Chelton et al.* [2003][d]
5.5°N	60	45	75	1992–2001	170°E–125°W	*Chelton et al.* [2003][e]
5.0°N	60	NA	NA	1992–1996	160°E–85°W	*Susanto et al.* [1998][f]
7.0°N	50	NA	NA	1976–1985	125°E–175°E	*Mitchum and Lukas* [1990][g]
6.0°N	50	NA	NA	pre-1979	140°E–80°W	*Meyers* [1979][h]
5.5°S	45	38	65	1993–2006	160°E–95°W	30-day boxcar[b]
5.5°S	46	38	71	1993–2006	160°E–95°W	500-day high pass[b]
5.5°S	43	37	57	1993–2001	160°E–95°W	30-day boxcar[b]
5.5°S	44	37	59	1993–2001	160°E–95°W	500-day high pass[b]
5.5°S	69	58	85	2001–2006	160°E–95°W	30-day boxcar[b]
5.5°S	71	57	87	2001–2006	160°E–95°W	500-day high pass[b]
5.5°S	31	23	39	1993–2006	170°W–140°W	30-day boxcar[b]
5.5°S	52	34	70	1994–2000	160°E–95°W	*Chelton et al.* [2003][c]
5.5°S	55	51	62	1994–2000	160°E–95°W	*Chelton et al.* [2003][d]
5.5°S	48	38	58	1992–2001	170°E–125°W	*Chelton et al.* [2003][e]
7.0°S	40	NA	NA	1992–1996	160°E–85°W	*Susanto et al.* [1998][f]

[a]Speed values are in cm s^{-1}. NA, not available.
[b]Minimum along-slope standard deviation.
[c]Hilbert transform CEOF analysis.
[d]Maximum cross correlation of time-lagged EOFs.
[e]Radon transform.
[f]Complex singular value decomposition.
[g]Complex demodulation.
[h]Maximum correlation between observations and expected response to Ekman pumping.

cases are similar (Table 2). As noted, the minimizations indicate similar predominant propagation speed over time at 5.5°N but show clear changes at 5.5°S, where the optimum phase speed identified over 2001–2006 is significantly faster than the speeds over 1993–2001 or the entire 1993–2006 period. Such interannual variability will contribute to differences in studies over different time periods.

[48] Westward propagation speeds determined from the various analyses of the MODAS SSH time series are presented for comparison with similar examinations from other studies in Table 2. The along-slope standard deviation exhibits little sensitivity to the preprocessing filters applied, as the results using the 500-day high-pass filter are very similar to those using the 30-day boxcar filter, within 1–2 cm s^{-1} in all cases. Results are significantly different between the sections over 170°W–140°W and 160°E–95°W, with the narrower, centrally located section examined earlier in this paper having prevailing phase speeds significantly slower than the average across the broader near-equatorial Pacific.

[49] *Chelton et al.* [2003] applied different approaches and data subsets to identify predominant speeds of westward propagation. In the first approach, they identified the dominant Hilbert transform complex EOF (CEOF) of filtered SSH in a band between 15°N and 15°S from 160°E to 95°W. Data covered January 1994 to December 1999, rounded to indicate 1994–2000 in Table 2. This CEOF accounted for 67% of the observed variance in the filtered SSH. The authors extracted the phase of the CEOF along 5.5°N and 5.5°S. Phase speed was estimated as the reciprocal of the spatial slope of CEOF phase variation. Using the same space and time subset in an alternate approach, *Chelton et al.* [2003] fit EOFs to height (h) and corresponding geostrophic velocity components (u, v). Prevalent phase speeds averaged over the band were identified by the maximum time-lagged cross correlation of the EOF functions. The h, u, and v EOFs produced slightly different results, accounting for the uncertainty range in Table 2. As a third option, *Chelton et al.* [2003] applied a Radon transform [*Deans*, 1983] to a slightly different data subset, an SSH time series from November 1992 to May 2001 with the zonal range limited to 170°E–125°W. The narrower transect excludes faster phase speeds in the far west that might unduly bias the result. Although the Radon transform did not have a formal statistical definition for its uncertainty range, the range of speeds with transform values within 95% of the maximum was taken as a useful uncertainty estimate.

[50] Other studies examine alternative objective methods. For example, *Susanto et al.* [1998] passed altimeter data through a moving average and median filter before applying complex singular value decomposition. Rossby wave phase speed was estimated by the temporal phase function of the first EOF mode. Sea level data from a line of Pacific tide stations near 7°N are the foundation for a study by *Mitchum and Lukas* [1990] in which complex demodulation was used to represent the evolution of the annual phase and amplitude of sea level variability, thereby identifying a westward

phase propagation near 50 cm s^{-1}. In the earliest study included here, *Meyers* [1979] used a gridded monthly climatology of bathythermograph observations to map the typical annual evolution of the 14°C isotherm. His estimate of a 50 cm s^{-1} westward phase speed was based on maximum correlation between observed variations and the expected thermocline response to Ekman pumping. No uncertainty estimates were provided with these latter three methods.

[51] Results from several studies in the near-equatorial Pacific have been included in Table 2 for comparison. These employed a wide variety of techniques to estimate predominant westward propagation speeds over different zonal ranges and time intervals. The estimates using minimization of along-slope standard deviation are in general agreement with assessments by the various other techniques. The other studies on average estimate slightly faster speeds. The average speed reported from other sources is 55 cm s^{-1} (49 cm s^{-1}) near 5.5°N (5.5°S), an increase of 15% (9%) relative to along-slope minimization results using the 30-day boxcar filter over 1993–2006. The various reported values generally fall within the predicted range of uncertainty. Interannual variability can play a larger role, as shown near 5.5°S, where speeds calculated from 2001 to 2006 are over 50% larger than the 1993–2006 mean and 40% larger than the mean from other studies. Dominant phase speeds also differ over different sections at the same latitude; at 5.5°N the dominant speeds over the section 160°E–95°W are about 30% larger than speeds over the narrower 170°W–140°W section. These comparisons in the central Pacific demonstrate the reliability of both the minimization of along-slope standard deviation technique and the gridded SSH products for examination of westward propagation.

7. Conclusions

[52] A new objective method to estimate prevailing eddy and Rossby wave propagation speeds is introduced and applied to SSH time series along Pacific sections extracted from daily global MODAS SSH analyses. The objective method based on minimizing along-slope standard deviation within the time series data array has been demonstrated to be a robust and useful approach. It produces impartial estimates that are accurate, reproducible, and have a well-defined prediction uncertainty. Its results are consistent with subjective estimates over a large range of the central North and South Pacific and are in general agreement with a variety of studies in the near-equatorial Pacific. Paired with the archive of daily MODAS global SSH analyses, it is equally applicable for other areas of global ocean. The techniques and data used will likely prove useful in further examinations of signal propagation and ocean circulation.

[53] An alternative derivation of the along-slope minimization shows that it can be understood in terms of an extension of the Radon transform that returns mean along-slope standard deviation as a function of projection angle. To verify this, a Radon transform code was modified to compute a R_{NRL} solution as in equation (5). Applied to the data for Figure 7a and sampling θ at 1° intervals, the cost function $J(\theta)$ returned a minimum at $\theta = 169°$. Equation (14) returns a corresponding dominant phase speed of 5.7 cm s^{-1}, in good agreement with the 5.9 cm s^{-1} (5.3–7.0 cm s^{-1}) estimate and uncertainty range returned by the more precise initial algorithm used for other calculations in the paper. For context, angles of 168° and 170° correspond to speeds of 6.2 cm s^{-1} and 5.1 cm s^{-1}, showing the precision of 1° angular increments. A more comprehensive R_{NRL} algorithm would need much finer angular increments to achieve the precision of the initial method that examines all possible slopes resolved in the grid. However, since it considers far fewer angles and makes other approximations, the simplified R_{NRL} algorithm is much faster than the full along-slope minimization. To improve calculation efficiency, the standard along-slope minimization considers only angles corresponding to westward propagation. The R_{NRL} algorithm can detect eastward or westward propagation, as demonstrated by reversing the longitudes in the 25°N section. Applying R_{NRL} to this reversed data returns the same 5.7 cm s^{-1} propagation speed directed to the east.

[54] While the subjective phase speed determination is easily implemented, it is subject to the biases of the human analyst and at the extremes could lead to cases of pathological science [*Langmuir*, 1989] where the analyst becomes convinced of results that are really random in nature. Used in conjunction with along-slope minimization, the subjective speed estimates can identify possible trends outside the dominant patterns, perhaps because of a secondary effect. In turn, the objective error bounds help identify cases where subjective interpretations should be considered with increased skepticism. This additional information on the uncertainty would be useful in resolving alternate subjective interpretations by different analysts. The more robust definition of error bounds is also an advantage of the along-slope minimization relative to some of the alternate objective techniques used in prior studies.

[55] Speed evaluations over a series of central Pacific sections show a fairly symmetric decrease from above 30 cm s^{-1} within 10° of the equator to below 1 cm s^{-1} at ±50°. The band closest to the equator contains the largest speeds and largest deviations from symmetry, 31 cm s^{-1} at 5.5°S and about 5 cm s^{-1} faster at 5.5°N. The speed estimates are sensitive to the width of the section, with prevailing speeds 25–30% lower over 170°W–140°W than over the broader 160°E–95°W sections. Using the latter sections, results (error bounds) of 48 cm s^{-1} (42–55 cm s^{-1}) at 5.5°N and 45 cm s^{-1} (58–85 cm s^{-1}) at 5.5°S are consistent with several prior studies over similar sections. Additional differences likely arise from the variety of observation systems used in the various studies and the assumptions regarding error covariances or other aspects of data interpolation or averaging, but the influence of these factors is relatively small as results from these different studies generally agree within the standard error, as shown above.

[56] The data and methods presented here may assist in regionally identifying dynamic balances leading to the observed propagation: nondispersive Rossby waves, free eddies, interaction with background flow, etc. The along-slope minimization is generally applicable for examining propagation of signals in other settings or disciplines. For example, an irregular array of sea level gauges along a coast could observe the passage of a Kelvin wave. By arranging the data in a Hovmöller diagram with distance along the

coast the x axis and time on the y axis, the minimum along-slope standard deviation would correspond to the reciprocal of the mean phase speed of the Kelvin wave as it propagates along the coast. Alternatively, the northward component of SSH propagation in the open ocean could be assessed over a series of meridional sections, although *Glazman and Weichman* [2005] report that this approach has not been very successful as it resolves only one component of the velocity field and it has difficulty isolating a dominant signal among superimposed northward and southward propagation. Such applications may be evaluated in a subsequent study.

[57] The along-slope minimization or equivalent R_{NRL} transform identify the prevailing westward propagation of sea surface height. The method does not distinguish the mechanism for the propagation, just the fact that there is a dominant signal. In a hypothetical situation where multiple processes are producing westward propagation at different speeds, the method identifies the speed that produces an overall minimization of standard deviation traveling with the signal and does not necessarily identify distinct peaks for different signals, although in an ideal case perhaps multiple local minima would emerge with one being selected as the overall dominant phase. Thus the method only finds the dominant signal propagation, one piece of evidence that must be combined with other observations or theoretical considerations to support interpretation as a Rossby wave, eddy, or other process. We have also demonstrated one use of the gridded global SSH fields; their global coverage and high resolution in space and time make them useful for a variety of other applications.

Appendix A: SSH Determination by Altimeters

[58] ALPS transforms GDRs through five steps, involving initial data processing, interpolation, tide removal, orbit error removal, and referencing to a consistent mean. Processing in ALPS is designed to reveal the steric component of SSH, as this is the SSH signal that is related to subsurface structure through changes in vertically integrated specific volume. Alternative approaches might be appropriate if another signal is of interest.

[59] Initial processing applies atmospheric corrections to yield a more accurate estimate of the distance between the altimeter and the sea surface. Altimeters measure the two-way travel time of microwave signals reflected from the sea surface. The distance between the satellite and the ocean surface equals half the travel time times the average speed of light along the signal path. Corrections including dry troposphere path delay, wet troposphere path delay, ionosphere path delay, and electromagnetic bias correction terms are applied to more accurately estimate microwave speed. These calculations give an accurate distance between the altimeter and the sea surface.

[60] The second element is an accurate determination of altimeter position relative to the local geoid. This orbit solution is one of the largest error sources associated with real time altimeter data. Its determination begins with time averaging the altimeter record to 1 s intervals and standard exact repeat locations along the ground track. The tidal component of SSH predicted by the global tide model is removed at each location. Orbit error removal is done on one satellite revolution's worth of data at a time using a weighted least squares technique, with weighting based on the variability observed by prior altimeter missions. This minimizes the impact of large amplitude features in areas dominated by mesoscale variability. The Navy Generalized Digital Environmental Model (GDEM) climatology [*Teague et al.*, 1990] is used to maintain the seasonal steric signal in the SSH data while removing orbit errors.

[61] The exact repeat orbits enable the position of the satellite relative to the geoid to be determined with higher precision than would be possible with individual orbits. The mean height of multiple repeat orbits and the height difference of one pass relative to this multiple-orbit mean can be determined with much greater precision than the individual geoids or orbit solutions. Crossover points are used to reference multiple altimeters to a common mean. Use of the height difference relative to the repeat orbit mean allows altimeter data to be used in oceanographic applications requiring precise SSH with a common global mean.

[62] The third element in determining SSH is to distinguish the contributions of various SSH components. With SSH defined as a height anomaly from a long-term mean, as indicated above, then total sea surface height is the sum of steric and nonsteric components. Steric SSH encompasses changes in vertically integrated specific volume due to changes in temperature and salinity without changes in vertically integrated mass. Nonsteric SSH components are due to changes in vertically integrated mass. Our application of altimeter height needs only the steric component of SSH, the component correlated with subsurface anomalies of temperature and salinity [*Fox et al.*, 2002]. Thus, in the ALPS signal processing, we estimate and remove nonsteric height contributions due to tides or the static inverse barometer response to atmospheric pressure as described by *Barron et al.* [2004], in detail.

[63] **Acknowledgments.** We would like to thank Kirk Whitmer (formerly of NRL) and Robert Broome of Planning Systems Inc. for their work on processing the altimeter data, Jan Dastugue of NRL for her help in developing and maintaining the MODAS Web site, and Mike Carnes of NRL for referring us to the digitized gravity wave phase speed data. We thank our two anonymous reviewers for their constructive comments and suggestions. This work is funded by the Office of Naval Research under the 6.2 project Improved Synthetic Ocean Properties. The paper is contribution NRL/JA/7320/08/8241 and has been approved for public release.

References

Barron, C. N., and A. B. Kara (2006), Satellite-based daily SSTs over the global ocean, *Geophys. Res. Lett.*, *33*, L15603, doi:10.1029/2006GL026356.

Barron, C. N., A. B. Kara, H. E. Hurlburt, C. Rowley, and L. F. Smedstad (2004), Sea surface height predictions from the global Navy Coastal Ocean Model (NCOM) during 1998–2001, *J. Atmos. Oceanic Technol.*, *21*, 1876–1894.

Boebel, O., and C. Barron (2003), A comparison of in-situ float velocities with altimeter derived geostrophic velocities, *Deep Sea Res., Part II*, *50*, 119–139.

Bowling, D., G. Starr, J. Wood, and R. Lumia (2007), Wide band suppression of motion-induced vibration, in *2007 IEEE International Conference on Robotics and Automation*, pp. 4530–4536, Inst. of Electr. and Electr. Eng., New York.

Challenor, P. G., P. Cipollini, and D. Cromwell (2001), Use of the 3D Radon transform to examine the properties of oceanic Rossby waves, *J. Atmos. Oceanic Technol.*, *18*, 1558–1566.

Challenor, P. G., P. Cipollini, D. Cromwell, K. L. Hill, G. D. Quartly, and I. S. Robinson (2004), Characteristics of mid-latitude Rossby wave propagation from multiple satellite datasets, *Int. J. Remote Sens.*, *25*, 1297–1302.

Chambers, D. P., J. C. Ries, and T. J. Urban (2003), Calibration and verification of Jason-1 using global along-track residuals with TOPEX, *Mar. Geod.*, *26*, 305–317.

Chelton, D. B., and M. Schlax (1996), Global observations of oceanic Rossby waves, *Science*, *272*, 234–238.

Chelton, D. B., R. A. de Szoeke, M. G. Schlax, K. El Naggar, and N. Siwertz (1998), Geographical variability of the first-baroclinic Rossby radius of deformation, *J. Phys. Oceanogr.*, *28*, 433–460.

Chelton, D. B., M. G. Schlax, J. M. Lyman, and G. C. Johnson (2003), Equatorially trapped Rossby waves in the presence of meridionally sheared baroclinic flow in the Pacific Ocean, *Prog. Oceanogr.*, *56*, 323–380.

Chelton, D. B., M. G. Schlax, R. M. Samelson, and R. A. de Szoeke (2007), Global observations of large oceanic eddies, *Geophys. Res. Lett.*, *34*, L15606, doi:10.1029/2007GL030812.

Cipollini, P., D. Cromwell, M. S. Jones, G. D. Quartly, and P. G. Challenor (1997), Concurrent altimeter and infrared observations of Rossby wave propagation near 34° in the northeast Atlantic, *Geophys. Res. Lett.*, *24*, 889–892.

Cushman-Roisin, B., E. P. Chassignet, and B. Tang (1990), Westward motion of mesoscale eddies, *J. Phys. Oceanogr.*, *20*, 758–768.

Deans, S. R. (1983), *The Radon Transform and Some of Its Applications*, 289 pp., John Wiley, New York.

Dunkerton, T. J., and F. X. Crum (1995), Eastward propagating ∼2- to 15-day equatorial convection and its relation to the tropical intraseasonal oscillation, *J. Geophys. Res.*, *100*, 25,781–25,790.

Emery, W. J., and L. Magaard (1976), Baroclinic Rossby waves as inferred from temperature fluctuations in the eastern Pacific, *J. Mar. Res.*, *34*, 365–385.

Fox, D. N., W. J. Teague, C. N. Barron, M. R. Carnes, and J. V. Gurley (2002), The Modular Ocean Data Assimilation System (MODAS), *J. Atmos. Oceanic Technol.*, *19*, 240–252.

Gill, A. E. (1982), *Atmosphere-Ocean Dynamics*, *Int. Geophys. Ser.*, vol. 30, 662 pp., Academic, San Diego, Calif.

Glazman, R. E., and P. B. Weichman (2005), Meridional component of oceanic Rossby wave propagation, *Dyn. Atmos. Oceans*, *38*, 173–193.

Jacobs, G. A., W. J. Emery, and G. H. Born (1993), Rossby waves in the Pacific Ocean extracted from Geosat altimeter data, *J. Phys. Oceanogr.*, *23*, 1155–1175.

Jacobs, G. A., C. N. Barron, and R. C. Rhodes (2001), Mesoscale characteristics, *J. Geophys. Res.*, *106*, 19,581–19,595.

Killworth, P. D., D. B. Chelton, and R. A. de Szoeke (1997), The speed of observed and theoretical long extratropical planetary waves, *J. Phys. Oceanogr.*, *27*, 1946–1966.

Langmuir, I. (1989), Pathological science, *Phys. Today*, *10*, 36–48.

Legeckis, R. (1977), Long waves in the eastern equatorial Pacific Ocean: A view from a geostationary satellite, *Science*, *197*, 1179–1181.

Lorenc, A. C. (1981), A global three-dimensional multivariate statistical interpolation scheme, *Mon. Weather Rev.*, *109*, 701–721.

Meyers, G. (1979), Annual Rossby wave in the tropical North Pacific Ocean, *J. Phys. Oceanogr.*, *4*, 663–674.

Mitchum, G. T., and R. Lukas (1990), Westward propagation of annual sea level and wind signals in the western Pacific Ocean, *J. Clim.*, *3*, 1102–1110.

Nof, D. (1981), On the β-induced movement of isolated baroclinic eddies, *J. Phys. Oceanogr.*, *11*, 1662–1672.

Osychny, V., and P. Cornillon (2004), Properties of Rossby waves in the North Atlantic estimated from satellite data, *J. Phys. Oceanogr.*, *34*, 61–76.

Rossby, C. G. (1939), Relation between variations in the intensity of the zonal circulation of the atmosphere and the displacements of the semi-permanent centers of action, *J. Mar. Res.*, *2*, 38–55.

Susanto, R. D., Q. Zheng, and X.-H. Yan (1998), Complex singular value decomposition analysis of equatorial waves in the Pacific observed by TOPEX/POSEIDON altimeter, *J. Atmos. Oceanic Technol.*, *15*, 764–774.

Teague, W. J., M. J. Carron, and P. J. Hogan (1990), A comparison between the Generalized Digital Environmental Model and Levitus climatologies, *J. Geophys. Res.*, *95*, 7167–7183.

White, W. B. (1977), Annual forcing of baroclinic long waves in the tropical North Pacific Ocean, *J. Phys. Oceanogr.*, *7*, 50–61.

Whitmer, K. R., G. A. Jacobs, and O. M. Smedstad (2004), Altimeter signal-to-noise for deep ocean processes in operational systems, *Mar. Geod.*, *27*, 433–451, doi:10.1080/01490410490902007.

Zlotnicki, V., L.-L. Fu, and W. Patzert (1989), Seasonal variability in global sea level observed with Geosat altimetry, *J. Geophys. Res.*, *94*, 17,959–17,969.

C. N. Barron, G. A. Jacobs, and A. B. Kara, Oceanography Division, Naval Research Laboratory, Code 7320, Building 1009, Stennis Space Center, MS 39529, USA. (charlie.barron@nrlssc.navy.mil)